

EVOLUTION OF THE MERGER INDUCED HYDROSTATIC MASS BIAS IN GALAXY CLUSTERS

KAYLEA NELSON¹, DOUGLAS H. RUDD^{2,3}, LAURIE SHAW^{2,3}, DAISUKE NAGAI^{1,2,3}

ACCEPTED TO APJ: *March 22, 2012*

ABSTRACT

In this work, we examine the effects of mergers on the hydrostatic mass estimate of galaxy clusters using high-resolution Eulerian cosmological simulations. We utilize merger trees to isolate the last merger for each cluster in our sample and follow the time evolution of the hydrostatic mass bias as the systems relax. We find that during a merger, a shock propagates outward from the parent cluster, resulting in an overestimate in the hydrostatic mass bias. After the merger, as a cluster relaxes, the bias in hydrostatic mass estimate decreases but remains at a level of -5–10% with 15–20% scatter within r_{500} . We also investigate the post-merger evolution of the pressure support from bulk motions, a dominant cause of this residual mass bias. At r_{500} , the contribution from random motions peaks at 30% of the total pressure during the merger and quickly decays to $\sim 10\text{--}15\%$ as a cluster relaxes. Additionally, we use a measure of the random motion pressure to correct the hydrostatic mass estimate. We discover that 4 Gyr after mergers, the direct effects of the merger event on the hydrostatic mass bias have become negligible. Thereafter, the mass bias is primarily due to residual bulk motions in the gas which are not accounted for in the hydrostatic equilibrium equation. We present a hydrostatic mass bias correction method that can recover the unbiased cluster mass for relaxed clusters with 9% scatter at r_{500} and 11% scatter in the outskirts, within r_{200} .

Subject headings: cosmology: theory galaxies: clusters: general

1. INTRODUCTION

Over the last decade, measurements of the abundance of galaxy clusters have begun to provide important constraints on cosmological parameters (Vikhlinin et al. 2009; Mantz et al. 2010; Rozo et al. 2009; Vanderlinde et al. 2010; Sehgal et al. 2010). Clusters trace the highest peaks in the matter density field; their abundance as a function of mass and redshift is therefore extremely sensitive to the growth rate of density perturbations as well as the expansion rate of the Universe.

The power of cluster number counts as a cosmological probe is principally limited by the accuracy with which their total mass can be measured. Cluster mass can be estimated using a wide variety of techniques, from measurements of the number or velocity dispersion of the cluster member galaxies, strong and weak gravitational lensing of background sources, and measurements of their X-ray emission or Sunyaev-Zel'dovich (SZ) signal. The two latter methods utilize the temperature and density of the hot plasma, or intra-cluster medium (ICM), that pervades cluster environments and dominates their baryonic mass. The thermal properties of the ICM are very sensitive to the depth of the gravitational potential of the cluster host dark matter halo, and therefore to the total cluster mass. In particular, by measuring the radial density and temperature profiles of the ICM from X-ray and SZ observations, the equation of hydrostatic equilibrium (HSE) can be solved to obtain the total matter profile.

Application of the equation of HSE is based on the assumption that the ICM is both spherically symmetric

and in hydrostatic equilibrium. However, clusters are dynamically young systems and obtain a significant fraction of their mass through mergers. Therefore the accuracy of this assumption must be questioned. Recent cosmological simulations have suggested that even in relaxed clusters the HSE method may systematically underestimate the total cluster mass by $\sim 10\text{--}20\%$ (Kay et al. 2004; Rasia et al. 2006; Nagai et al. 2007b). It has been demonstrated that this bias is a consequence of neglecting the contribution of residual bulk motions in the ICM to the dynamical stability of relaxed clusters (Kay et al. 2004; Rasia et al. 2004; Jeltema et al. 2008; Piffaretti & Valdarnini 2008; Lau et al. 2009). Typically, the HSE technique only accounts for support from thermal pressure; the non-thermal contribution from bulk motions and turbulence is difficult to measure directly. The evolution of these bulk motions, their generation through mergers, and the potential effect on the corresponding evolution of the mass bias are all very poorly understood.

Several recent works use cosmological simulations of clusters to investigate the effects of dynamical state on the deviation from hydrostatic equilibrium by examining a number of clusters at single redshifts. Nagai et al. (2007b) demonstrate that the mass bias increases rapidly with radius and is 20% or greater at all radii in unrelaxed systems. Utilizing a large sample of over 100 clusters, Piffaretti & Valdarnini (2008) show that the hydrostatic mass bias is larger for the less relaxed, recently merged clusters, and also that the scatter in the bias increases with the degree of disturbance in the systems.

In an attempt to incorporate observational uncertainties, Meneghetti et al. (2010) investigate the effect of line of sight projections using mock lensing and mock X-ray observations and were able to recover the bias measured directly in simulations. In an extension of Meneghetti et al. (2010), Rasia et al. (2012) also investigate the ef-

kaylea.nelson@yale.edu

¹ Department of Astronomy, Yale University, New Haven, CT, 06520

² Department of Physics, Yale University, New Haven, CT 06520

³ Yale Center for Astronomy & Astrophysics, Yale University, New Haven, CT 06520

fects of cluster morphology, environment, temperature inhomogeneity, and mass on the mass biases. Moreover, both works show agreement with an observational comparison of the X-ray hydrostatic mass estimate and weak lensing mass estimates by Mahdavi et al. (2008), namely that the HSE mass derived from *Chandra* X-ray measurements is biased low by $\sim 20\%$ at r_{500} ⁴ compared to weak gravitational lensing measurements. Similarly, Zhang et al. (2010) investigate the effect of dynamical state on the bias between the mass measurement methods and find a $\sim 10\%$ underestimate in the HSE mass at r_{500} in undisturbed clusters but also find that in disturbed clusters the mass is overestimated by $\sim 6\%$ at the same radius.

In this paper, we use high-resolution cosmological simulations to investigate the time evolution of the hydrostatic mass bias and non-thermal pressure support in the ICM as a function of time since the latest merger. While a number of recent studies have explored the effects of mergers and dynamical state on the hydrostatic mass estimate (e.g. Kay et al. 2004; Rasia et al. 2006; Nagai et al. 2007b; Lau et al. 2009; Poole et al. 2006; Piffaretti & Valdarnini 2008), most only explored these effects at a single epoch or in idealized mergers. Our simulations and merger trees enable us to characterize the dynamical state of clusters robustly and quantitatively, and more effectively follow the evolution of the hydrostatic mass estimate during and after mergers in the context of realistic cosmological simulations. We investigate the source of the hydrostatic mass bias by following the post-merger evolution of the non-thermal pressure component of the ICM contributed primarily by random gas motions⁵. We find that during mergers, the bulk motions supply about 30% of the pressure support in clusters within r_{500} . While the random motion pressure quickly decays, we also find that after 9 Gyr, these gas motions still provide about 10% of the pressure support. By taking the random motion pressure into account in a correction factor, we are able to recover the true mass of relaxed clusters, clusters which have not undergone a merger in more than 4 Gyr, to within a few percent. We conclude by presenting a potential method for estimating this correction factor using the thermal pressure profile.

In Section 2, we describe our cosmological cluster simulations. In Section 3, we present our analysis of the time evolution of the hydrostatic mass bias. In Section 4 we explore the connection between non-thermal pressure and present our model for correcting the mass bias. In Section 5, we summarize and discuss our findings.

2. SIMULATIONS

We analyze a sample of 16 simulated groups and clusters of galaxies presented previously in Nagai et al. (2007b) and Nagai et al. (2007a), and we refer the reader to these papers for more details. We briefly summarize the relevant parameters of the simulations here.

The simulations are performed using the Adaptive Refinement Tree (ART) N -body+gas-dynamics code

⁴ Throughout this paper, we refer to total mass and ICM properties within radii which correspond to fixed overdensities Δ relative to the critical density at that redshift, such that $M_\Delta(r_\Delta) = \Delta(4/3)\pi r_\Delta^3 \rho_c(z)$.

⁵ Additional contributions from cosmic rays and magnetic field are not included.

TABLE 1
LIST OF SIMULATED CLUSTERS

Name ¹	r_{500} (h^{-1} Mpc)	M_{500} ($10^{14} h^{-1} M_\odot$)	t_{merger}^2 Gyr	Merger Ratio
CL101	1.128	8.31	2.19	0.49
CL102	0.967	5.24	3.09	0.27
CL103	0.975	5.37	2.00	0.81
CL104	0.970	5.29	8.72	0.24
CL105	0.902	4.26	8.53	0.21
CL106	0.854	3.61	1.64	0.31
CL107	0.766	2.60	5.98 ³	0.60
CL3	0.721	2.17	6.14	0.18
CL5	0.546	0.94	5.88	0.33
CL6	0.590	1.19	5.86	0.71
CL7	0.589	1.19	11.28	0.17
CL9	0.469	0.60	6.90	0.75
CL10	0.475	0.62	7.18	0.50
CL11	0.425	0.45	9.62	0.80
CL14	0.483	0.66	4.64	0.25
CL24	0.394	0.35	1.95	0.84

¹ Cluster labels correspond to those used in Nagai et al. (2007b).

² Time elapsed at $z = 0$ since last major merger.

³ At $z = 0$, CL107 is in the preliminary phases of a major merger with a halo that has not yet entered r_{200} and therefore is classified as an unrelaxed cluster despite having $t_{\text{merger}} = 5.98$ Gyr.

(Kravtsov 1999; Kravtsov et al. 2002; Rudd et al. 2008), which is an Eulerian code that uses adaptive refinement in space and time, and non-adaptive refinement in mass (Klypin et al. 2001) to achieve the dynamic range necessary to resolve the cores of halos formed in self-consistent cosmological simulations. The simulations assume a flat Λ CDM model: $\Omega_m = 1 - \Omega_\Lambda = 0.3$, $\Omega_b = 0.04286$, $h = 0.7$ and $\sigma_8 = 0.9$, where the Hubble constant is defined as $100h$ km s $^{-1}$ Mpc $^{-1}$, and σ_8 is the mass variance within spheres of radius $8 h^{-1}$ Mpc. The box size for CL101–CL107 is $120 h^{-1}$ Mpc comoving on a side and $80 h^{-1}$ Mpc comoving for CL3–CL24. All simulations were run using a uniform 128^3 grid with 8 levels of mesh refinement, corresponding to peak spatial resolution of $\sim 7 h^{-1}$ kpc and $5 h^{-1}$ kpc for the two box sizes respectively. Only the regions $\sim 3 - 10 h^{-1}$ Mpc surrounding each cluster center were adaptively refined. The dark matter (DM) particle mass in the region around each cluster was $m_p \approx 9.1 \times 10^8 h^{-1} M_\odot$ for CL101–CL107 and $m_p \approx 2.7 \times 10^8 h^{-1} M_\odot$ for CL3–CL24, while other regions were simulated with a lower mass resolution. In order to isolate the effect of mergers on the ICM we use simulations that treat only gravity and non-radiative hydrodynamics. Lau et al. (2009) show that the exclusion of cooling and star formation does not have a strong effect on the total contribution of gas motions to the HSE reconstruction of mass profiles outside of cluster cores.

Each cluster has 30 complete outputs in the range $z \leq 4$, with the majority occurring equally spaced in expansion factor after $z = 1$ with $\Delta a = \Delta(1+z)^{-1} = 0.025$. The dark matter particles, used to identify cluster mergers, are output at a much finer spacing with ≈ 300 outputs over the cluster history. This allows for a robust identification of the cluster progenitor and merger timing.

2.1. Halo Finder

A variant of the bound density maxima halo finding algorithm (Klypin et al. 1999) is used to identify halos and the subhalos within them. The details of the algorithm and parameters used in the halo finder can be found in

Kravtsov et al. (2004). The main steps of the algorithm are identification of local density peaks (potential halo centers) and analysis of the density distribution and velocities of the surrounding particles to test whether a given peak corresponds to a gravitationally bound clump. More specifically, we construct density, circular velocity, and velocity dispersion profiles around each center and iteratively remove unbound particles using the procedure outlined in Klypin et al. (1999).

2.2. Merger Trees

To examine the evolution of cluster properties and the hydrostatic mass bias, we track the evolution of each cluster’s most massive progenitor. We identify the main progenitor of each $z = 0$ cluster by iteratively following the 10% most bound dark matter particles at each epoch. Mergers are located by identifying objects that cross r_{200} of the parent cluster. We determine the mass ratio of the merger at an epoch when the two systems are sufficiently separated to avoid impacting their respective mass profiles, herein we use the epoch at which they initially overlap at a radius of r_{200} . We use the ratio of M_{500} at this epoch to identify major mergers, herein defined as a mass ratio greater than 1:6. Merging events with the mass ratios smaller than this are defined as minor mergers. While this ratio is somewhat lower than used in other studies (e.g. Gottlöber et al. 2001), careful exploration of the merger ratio has shown that this threshold best separates mergers that have a strong impact on the measured ICM properties from those that do not. We examine the evolution of these properties as a function of time since the last major merger, t_{merger} , defined as the epoch at which the center of the merging cluster first crosses r_{200} of the parent cluster.

2.3. Cluster Profiles

For each simulation output we measure properties of the ICM under the assumption of spherical symmetry following the methods described in Lau et al. (2009). A brief description of the methods used is included here. We focus in this work on the estimate of cluster mass provided by the thermal hydrostatic equilibrium equation,

$$M_{\text{HSE}}(< r) = -\frac{r^2}{G\rho_{\text{gas}}} \frac{dP_{\text{th}}}{dr}, \quad (1)$$

where $M_{\text{HSE}}(< r)$ is the estimated mass within radius, r , and $\rho_{\text{gas}}(r)$ and $P_{\text{th}}(r)$ are the gas density and thermal pressure, respectively. These are measured within spherical shells, logarithmically-spaced in radius from the cluster center.

We also measure the contribution of isotropic pressure from random gas motions,

$$P_{\text{rand}} = \frac{1}{3}\rho_{\text{gas}}(\sigma_r^2 + \sigma_t^2), \quad (2)$$

where σ_r^2 and σ_t^2 are radial and tangential velocity dispersions measured in spherical shells, using the peculiar velocity of the cluster dark matter within r_{500} to define a rest frame. In the absence of radiative cooling, rotational velocities are negligible outside $\sim 0.2r_{500}$, as was seen in Lau et al. (2009), however for completeness we treat their contribution to the effective pressure support separately.

Following Lau et al. (2009), we treat the random gas motions using approach similar to the treatment of the dynamical collisionless system using the Jeans equation (Binney & Tremaine 2008). The total mass of the cluster within a radius r can be split into separate components corresponding to different terms of the Jeans equation,

$$M_{\text{tot}}(< r) = M_{\text{HSE}} + M_{\text{rand}} + M_{\text{rot}}. \quad (3)$$

The streaming and cross terms are small, and we neglect them throughout this work. The rotational component, which contributes significantly to the pressure support in the core ($< 0.5 r_{500}$), is given by

$$M_{\text{rot}}(< r) = \frac{r\bar{v}_t^2}{G}, \quad (4)$$

where \bar{v}_t is the mean tangential velocity. The component from random gas motions is given by

$$M_{\text{rand}}(< r) = \frac{-r^2}{G\rho_{\text{gas}}} \left(\frac{\partial(\rho_{\text{gas}}\sigma_r^2)}{\partial r} \right) - \frac{r}{G}(2\sigma_r^2 - \sigma_t^2). \quad (5)$$

Note that spherical symmetry for the gravitational potential and steady state are assumed in deriving the expression for mass from the Jeans equation, and all the physical quantities at a given radius are averages over a radial shell.

To avoid biases due to the presence of substructure and to maintain consistency with Lau et al. (2009), in measuring M_{HSE} and P_{rand} we remove gas from within the tidal radius of subhalos of mass greater than $10^{12} h^{-1} M_\odot$. We further reduce small scale fluctuations in pressure and pressure gradient profiles by smoothing with a Savitzky-Golay filter. We have explicitly checked that neither subhalo removal nor smoothing procedures have a significant effect on our results.

It is important to note that all radial quantities in this paper, including M_{HSE} , are measured within the corresponding “true” radius, r_{true} , as measured directly from the simulations. Lau et al. (2009) shows that if M_{HSE} is instead measured within the radius as estimated from the HSE equation, r_{est} , the hydrostatic mass bias within r_{500} is increased by $\sim 4\%$ for relaxed systems (see also Nagai et al. 2007b, for results based on mock X-ray maps).

3. EVOLUTION OF THE HYDROSTATIC MASS BIAS

We begin by exploring in detail the evolution of a single object, CL10, with a relatively quiescent merger history prior to a major merger at $z \approx 0.72$. This allows us to isolate the effect of a single merger and compare directly to previous studies that explore idealized binary mergers (e.g., Ricker & Sarazin 2001; Poole et al. 2006).

The response of the ICM thermal pressure during the merger is illustrated by Figure 1. Each frame is $2h^{-1}$ Mpc comoving across and $1h^{-1}$ Mpc comoving deep in projection. r_{500} is marked with a thin white circle at each epoch, and $r_{200} \simeq 1.5r_{500}$ and $r_{2500} \simeq 0.5r_{500}$. Initially CL10 is very relaxed, not having experienced a merger for 4.2 Gyr. Note the nearly circular pressure contours within r_{500} in the first panel. The merging cluster, with mass ratio of 1:2, enters from the top of the frame with an orbit nearly in the plane of the projection, achieving closest approach approximately ~ 0.5 Gyr after the start of the merger. This naturally divides the merger

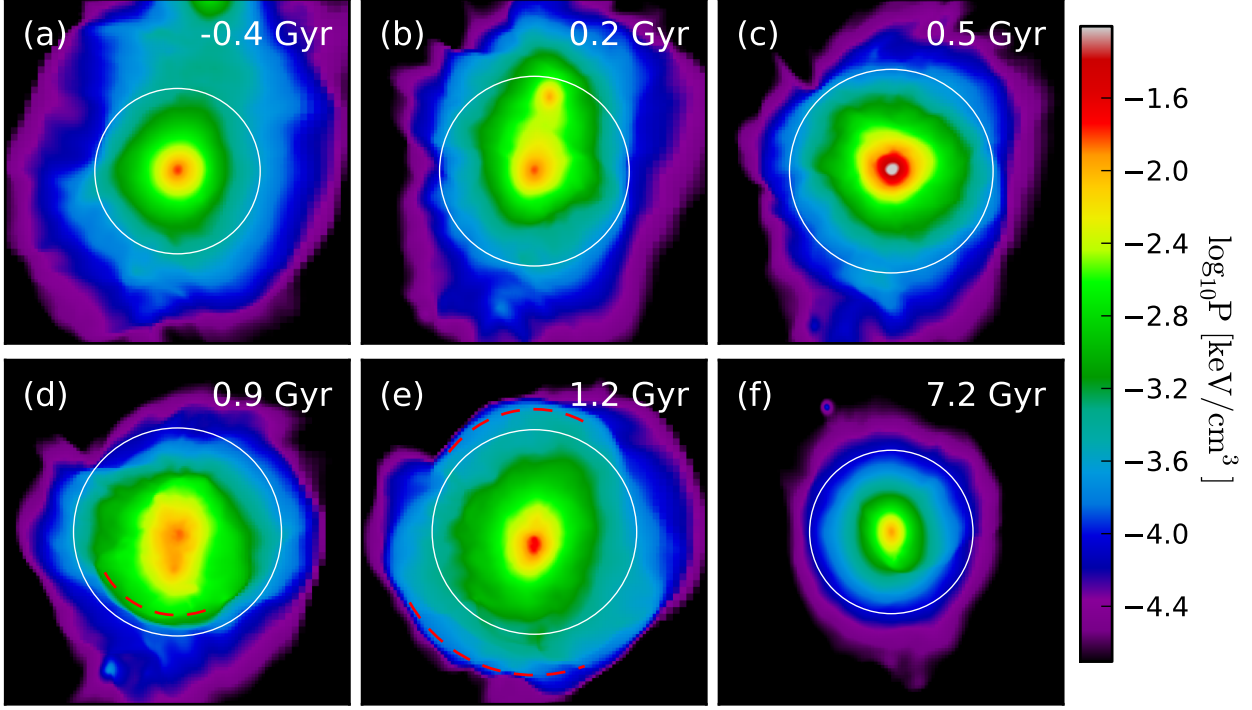


FIG. 1.— Thermal pressure maps of CL10 at six epochs surrounding the last major merger. Each panel is $2h^{-1}$ Mpc (comoving) and $1h^{-1}$ Mpc (comoving) along the line of sight, centered on the most massive progenitor. The white circles depict the size of r_{500} and the red dashed arcs mark the location of the merger shock. The time relative to the beginning of the merger (the epoch when the merging cluster cross r_{200}) is shown in each frame. Frame (b) shows the epoch when the merging cluster crosses r_{500} , frame (c) shows the time of closest approach, and frame (f) shows a time when CL10 has relaxed significantly after the merger.

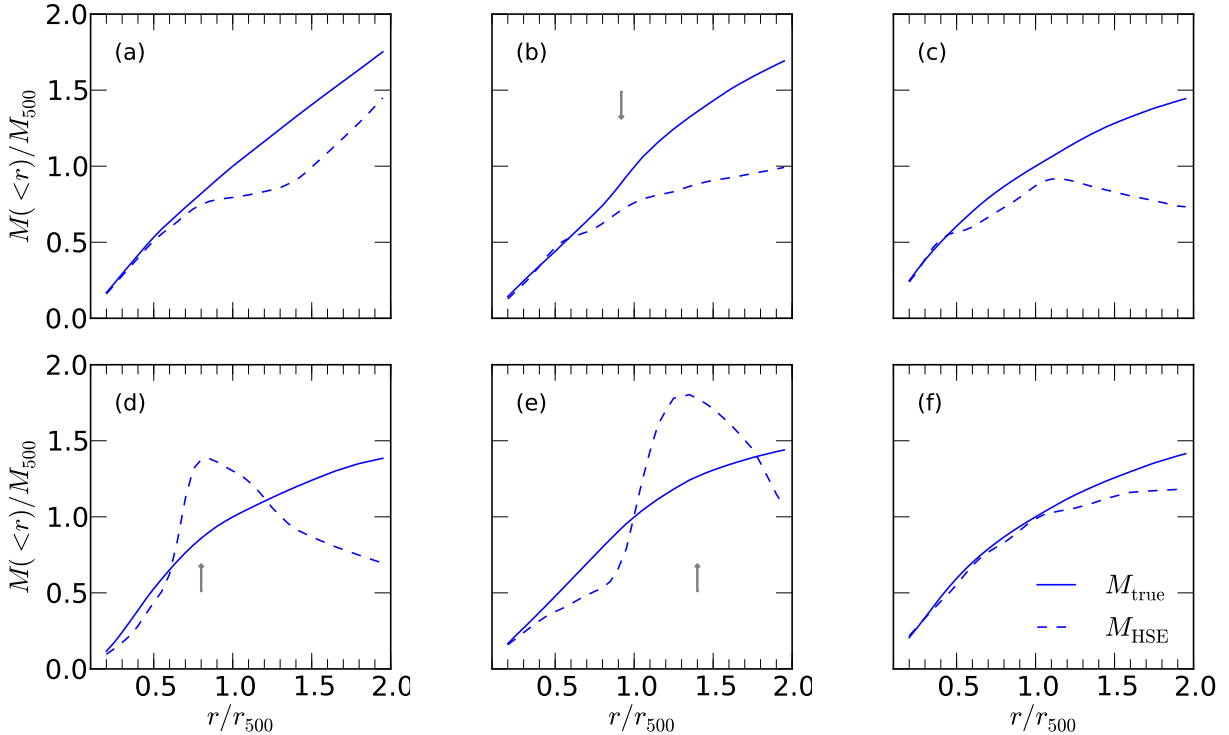


FIG. 2.— The mass profile of CL10 at the same six epochs depicted in Figure 1. The hydrostatic mass estimate, M_{HSE} , and the true mass, M_{true} , are shown by the dashed and solid lines, respectively. The downward facing arrow marks the location of the incoming merging halo. The upward facing arrow marks the location of the shock wave created by the merger as it emanates outwards through the parent halo.

into three epochs. In the initial passage (panels a–c) the spherically averaged outer pressure profile becomes shallower due to the presence of the merging cluster and compression of the ICM between the two cluster cores. At the time of closest approach the inner pressure profile becomes strongly peaked, generating forward and reverse merger shocks, marked with a dashed red arc (Ricker & Sarazin 2001). In this second phase of the merger (panels d and e), the merger shocks propagate outward, crossing r_{500} at ~ 0.9 Gyr following the start of the merger. After several sound crossing times the merger shocks have passed out of the cluster central region and merge with the large-scale accretion shock. The last panel of Figure 1 (f) shows CL10 at $z = 0$, ~ 7.2 Gyr after the merger. By this time the disruption of the merger has dissipated, leaving a relaxed, symmetric pressure profile similar to that seen at the start of the merger.

Deviations from hydrostatic equilibrium can be easily understood given the features seen in the pressure maps. In Figure 2, we compare the true mass profile (solid lines) to that predicted from the equation of hydrostatic equilibrium (Equation 1, dashed lines) at the same six epochs depicted in Figure 1. The start and end states are again qualitatively similar, with a cluster core in near-equilibrium and progressively greater deviation with increasing radius beyond r_{500} . The systematic underestimate of the total mass for relaxed clusters has been noted previously (Rasia et al. 2004; Nagai et al. 2007b; Lau et al. 2009).

The hydrostatic mass bias shows significant evolution in both radius and time. As the merging cluster makes its initial passage (panel b), with position denoted by the downward arrow, the true mass profile increases faster than the mass profile derived from the thermal pressure, temporarily increasing the (negative) hydrostatic mass bias at r_{500} .

The outwardly moving merger shocks, with approximate positions shown by upward arrows in panels (d) and (e), produce locally very steep pressure gradients, and thus strong overestimates of the true mass. This is seen as a positive peak in the hydrostatic mass bias profile that propagates outward with the shocks. The width of these peaks is caused by a combination of spherical averaging and the smoothing procedure described in Section 2. This evolution is in agreement with the evolution of the hydrostatic mass profile during a merging event shown in Puchwein & Bartelmann (2007).

The evolution of the hydrostatic mass bias at a fixed radius is governed by the radial migration of these features across that radius. Broadly, the bias will decrease slightly during the initial phase of the merger. As the merger shocks move outward the bias will see a dramatic rise, peaking at shock crossing before falling once more to a large negative bias. This bias will diminish at all radii as the cluster continues to relax from the inside-out, however, at $r \gtrsim r_{500}$ the bias persists to late times. As we will show in the next section, these features seen in the mass bias for the CL10 merger are generic to all the cluster mergers in our sample.

We now expand our exploration of the hydrostatic mass bias beyond the time immediately surrounding the CL10 merger. The top left panel of Figure 3 shows the evolution in the mass bias at 3 different radii, r_{2500} , r_{500} , and r_{200} , chosen for their relevance to X-ray and SZ ob-

servations. The bottom panel shows the mass accretion history at r_{500} normalized by the M_{500} at $z = 0$. A vertical line marks the beginning of the final major merger. The epochs shown in the previous figures are marked with red tick marks along the x-axes of the panels.

The final major merger (depicted in the previous figures) begins at ~ 6 Gyr. The mass of the cluster rises quickly as the incoming cluster merges with the parent cluster. About 1 Gyr after r_{200} crossing, we see another sharp, very positive bias in the top panel. The bias falls again and remains negative through $z = 0$, oscillating slightly as the cluster relaxes.

The evolution in the other radii is qualitatively similar, also showing the short-lived, positive bias immediately following the merger. Note that the peak at each radius occurs at a different time following the merger, with a delay of approximately ~ 0.5 Gyr between r_{2500} and r_{500} and between r_{500} and r_{200} , reflecting the shock propagation we observed in panels (d) and (e) of Figure 2. Immediately following the peak, the hydrostatic mass again underestimates the true mass and this negative bias holds but steadily diminishes to $z = 0$.

For comparison we also show in Figure 3 the evolution of two clusters selected from our full sample of 16. CL104 is a massive cluster that forms from a complicated triple merger at $z \approx 1.5$ and remains mostly quiescent thereafter. CL6 is intermediate in mass between CL10 and CL104, and experiences a nearly one-to-one merger at $z \approx 0.6$. Despite the differences in merger history and $z = 0$ mass, the clusters show remarkable similarity in their evolution. All three clusters have peaks ~ 1 Gyr following the identified merger, and show similar relative offsets between the different radii.

Cluster CL104 shows less prominent merger characteristics than seen in the other two clusters due to the triple merger, resulting in broader and smaller amplitude peaks at each radius. Following the major merger at $z \approx 1.5$, CL104 also undergoes a minor merger at $z \approx 0.25$. However, this merger only has a mass ratio of 10:1. Consequently the minor merger does not impact the cluster enough to have a significant effect on the mass estimate.

By $z = 0$, the mass bias for all three clusters approaches zero. However, it is important to note that even at $z = 0$ the hydrostatic mass bias within r_{500} is still biased low by 5–10% in the outskirts.

3.1. General Trends in the Hydrostatic Mass Bias

The post-merger evolution in Figure 3 exists for all 16 clusters in our simulated sample. This is shown explicitly in Figure 4, where the average evolution in the hydrostatic mass bias is plotted for the entire sample. The final major merger is identified for each cluster (see Table 1) and used to define a common point between clusters with varied accretion histories. The hydrostatic mass bias is measured at three separate radii, r_{2500} , r_{500} , and r_{200} , linearly interpolated to equally spaced times relative to the last major merger, and averaged over the entire sample. Error bars denote the error on the mean for r_{500} . The error bars for r_{2500} and r_{200} are comparable, and omitted for clarity. Note that clusters that undergo low-redshift mergers will only contribute to the low- t_{merger} portion of the figure. Consequently, while the behavior exhibited in the early epochs of Figure 4 is an average over the entire sample, the later epochs are

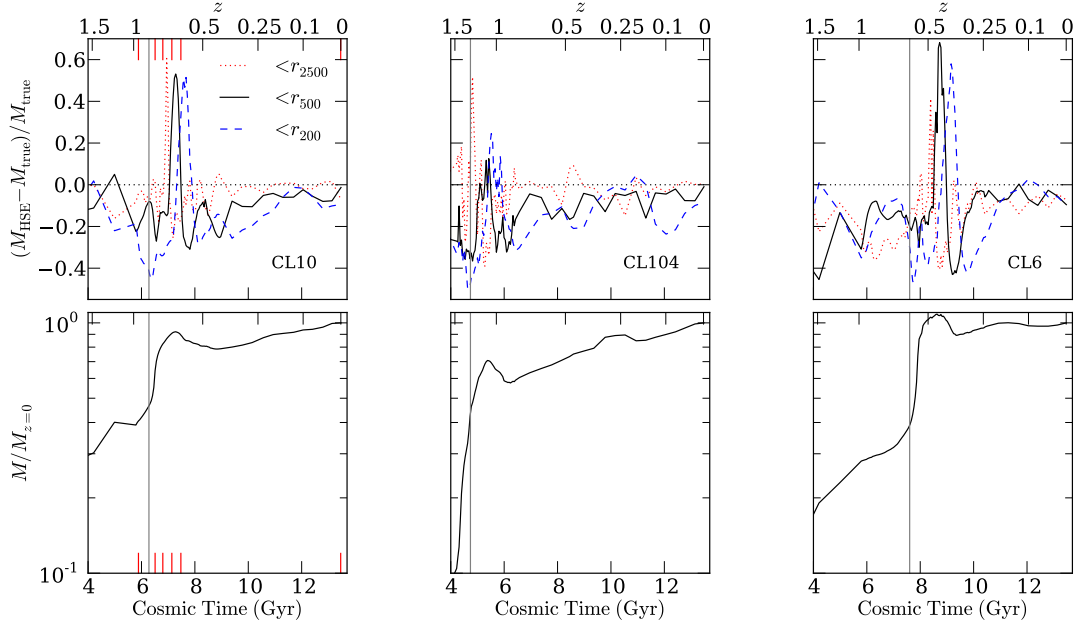


FIG. 3.— Top: The time evolution of the mass bias (top) for three clusters, CL10, CL104, and CL6 at three radii r_{2500} (red, dotted), r_{500} (black, solid), and r_{200} (blue, dashed). Bottom: The mass accretion history of the three clusters at r_{500} , normalized by M_{500} at $z = 0$. The vertical gray line marks the beginning of the latest major merger for each of the clusters. The red ticks mark the epochs in CL10 corresponding to the panels in Figures 1 and 2.

necessarily biased to a small number of early forming objects. We plot the evolution of the mass bias to 9.25 Gyr following the last merger at which point fewer than three clusters contribute to the average.

The qualitative features for the individual clusters presented in Figure 3 are also apparent in the sample-averaged evolution in Figure 4. Immediately preceding the merger, the hydrostatic mass underestimates the true mass by $\approx 10\%$ at all radii. This bias grows to nearly 30% in the outskirts shortly after the merger begins. Following the peaks associated with the merger shocks, the hydrostatic mass bias decreases over the subsequent 8 Gyr from $\sim 15\%-20\%$ to 3%, 10% and 18% within r_{2500} , r_{500} and r_{200} , respectively.

The peaks caused by the propagating merger shocks have smaller amplitude and are broader than the individual cluster histories seen in Figure 3. Therefore, the mean mass bias remains negative at all t_{merger} . This is caused by a variety of factors, including differences in the merger mass ratio and the orbital impact parameter, which changes the time offset between the peak and the start of the merger. Since the peaks are narrow in time (typically less than 0.5 Gyr), and we are primarily concerned with the average evolution after the merger, we make no attempt to reduce this broadening.

We also examined how the mass bias depended on various parameters, such as merger ratio, final cluster mass and redshift. We found little dependence on present mass of the cluster, with the larger clusters experiencing a slightly greater peak in the mass bias immediately following merger.

4. INFLUENCE OF NON-THERMAL PRESSURE ON THE HYDROSTATIC MASS BIAS

Figures 3 and 4 demonstrate that the magnitude of the mass bias decreases steadily following a merger, yet

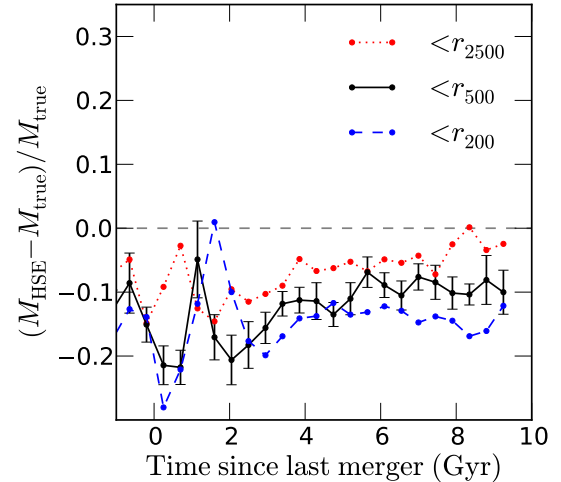


FIG. 4.— Averaged mass bias as a function of time elapsed since last merger (in Gyrs) for the sixteen clusters. A more detailed discussion of this figure is located in §3.1. The biases are plotted at radii r_{2500} (red, dotted), r_{500} (black, solid), and r_{200} (blue, dashed). The error bars show the 1σ error on the mean at r_{500} .

never fully disappears. If, as has been previously suggested (Lau et al. 2009; Nagai et al. 2007b; Rasia et al. 2004), residual motions in the ICM account for this bias, the non-thermal component of pressure due to these motions should see a similar evolution to the hydrostatic mass bias. We now investigate the evolution of this non-thermal component in more detail.

The top panels of Figure 5 show the evolving contribution of random motions to the total ICM pressure (left panel) and pressure gradient (right panel) averaged over

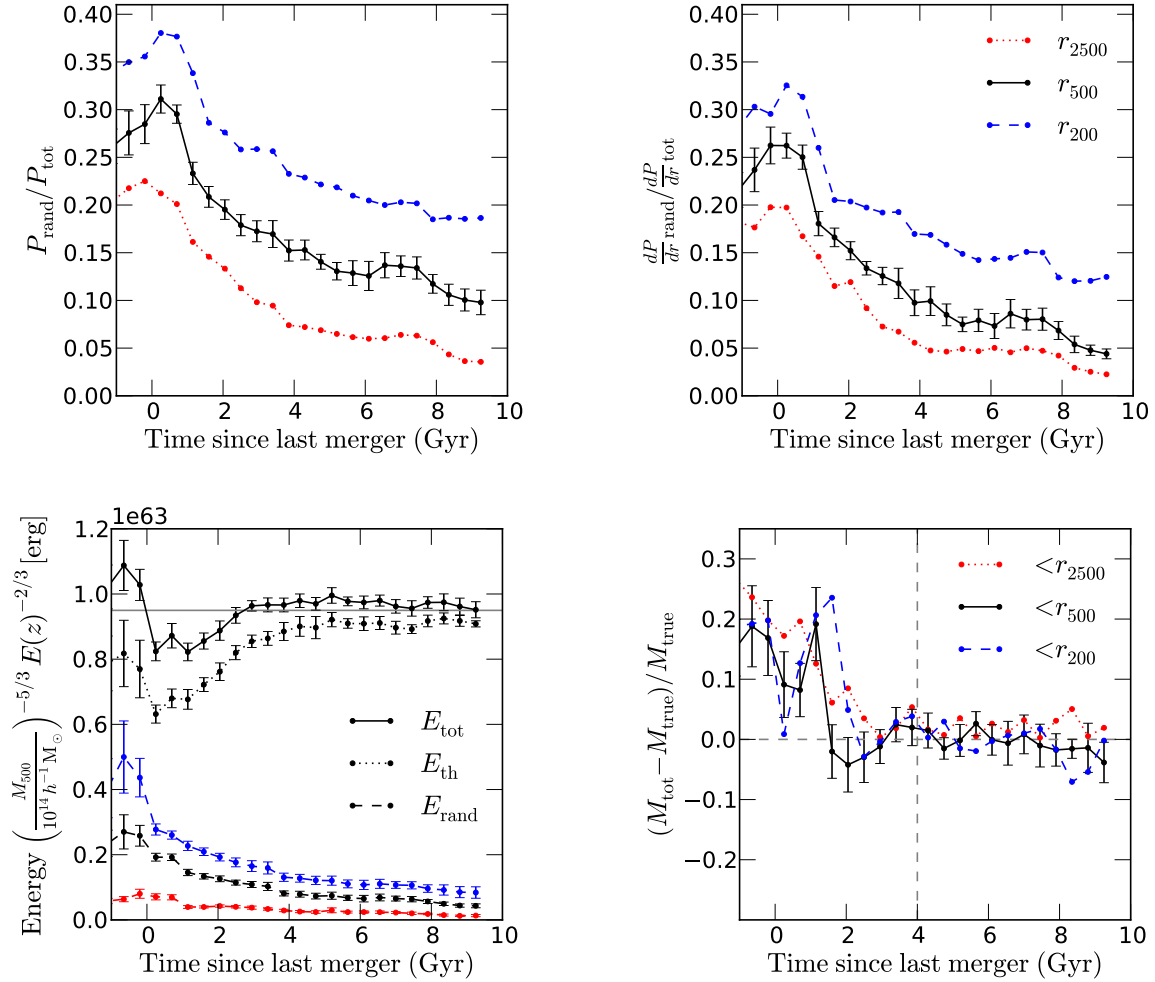


FIG. 5.— *Top:* Fractional contribution of random motions to the total effective pressure (left) and pressure gradient (right). *Bottom left:* The components of the total ICM energy. *Bottom right:* Averaged corrected mass bias as a function of time elapsed since last merger (in Gyrs) for the sixteen clusters. In all figures, the quantities are plotted at radii r_{2500} (red, dotted), r_{500} (black, solid), and r_{200} (blue, dashed). Our sample is divided into relaxed and unrelaxed clusters at $t_{\text{merger}} = 4$ Gyr (marked by the vertical dashed line). The error bars show the 1σ error on the mean at r_{500} .

all 16 clusters in the same manner as in Figure 4. The measurement of the non-thermal pressure support is described in Section 2.3. During the merger, the effective pressure from random motions is $\sim 30\%$ at r_{500} and has a strong trend with radius, increasing from $\sim 22\%$ at r_{2500} to $\sim 38\%$ at r_{200} . This radial trend persists throughout the merger and during the following relaxation. The non-thermal pressure fraction drops rapidly over the next 1–2 Gyr, and steadily decreases thereafter from $\sim 20\%$ to $\sim 10\%$ at r_{500} .

The radial pressure gradient shown in the top right panel of Fig. 5, an analog to the thermal pressure gradient in the equation of hydrostatic equilibrium (Eq. 1), shows similar trends in both radius and time since merger. Initially, random velocities contribute $\sim 20\%$, $\sim 26\%$, and $\sim 32\%$ to the non-thermal pressure gradient for r_{2500} , r_{500} , and r_{200} , respectively. This falls to between 2 – 12% after 8 Gyr, in line with the residual hydrostatic mass bias at those radii.

Our findings are consistent with the measurements of previous work. Lau et al. (2009) also sees small scatter

in the gradient of non-thermal pressure at r_{500} from 4–10% among clusters identified as relaxed at $z = 0$ and a larger range of 3–18% for unrelaxed clusters (see their Figure 3). While Lau et al. (2009) used the same simulations as this work, our mass biases are also in general agreement with the measurements from other simulations, e.g. GADGET-2 in Rasia et al. (2006); Piffaretti & Valdarnini (2008); Battaglia et al. (2011). The strong radial dependence in the non-thermal pressure fraction, with larger non-thermal support at greater radii is consistent with the results by Iapichino & Niemeyer (2008), Battaglia et al. (2011), and Vazza et al. (2011). In addition, the dependence on dynamical state seen in top panels of Figure 5 is consistent with the findings of Vazza et al. (2011). They also demonstrate that clusters undergoing mergers have a significantly larger fraction of non-thermal pressure support than relaxed or relaxing systems.

We expect the decay of the non-thermal component seen in the upper panels of Figure 5 is due to the conversion of random velocities to thermal energy via shocks

and numerical dissipation (no explicit physical viscosity was included in our simulations). Demonstrating this explicitly is difficult, however, as the total energy in the ICM increases by continued accretion subsequent to the merger, as can be seen in the bottom panels of Figure 3. To account for this growth we rescale the energy by the self-similar mass and redshift scaling $M^{5/3}E(z)^{2/3}$, where $E(z) = H(z)/H_0$ is the dimensionless Hubble constant (Kaiser 1986; Nagai et al. 2007a). In the bottom left panel of Figure 5 we show the evolution of the total (solid), thermal (dotted) and random kinetic (dashed) energy of the ICM within r_{500} , scaled by the self-similar expectation. To show the evolution of energy at different radii, we also plot the random kinetic energy within three radii: r_{2500} (red), r_{500} (black), and r_{200} (blue).

The total energy content of the ICM remains essentially constant beyond the 2 Gyr period following the merger. The time surrounding the merger shows a significant decrease in E_{tot} , however this is due not to a decrease in energy but rather the temporary increase in M_{500} caused by the presence of the merging cluster in the cluster core. Much of this mass will move to larger radius, decreasing the mean density and thus M_{500} , as can be seen in the accretion histories shown in Figure 3. The apparent decrease in energy is a reflection of this deviation from self-similarity, rather than a change in the total ICM energy. Since the total energy remains constant, we can associate directly the decrease in random kinetic energy with the increase in thermal energy. This thermalization is in agreement with the findings of Vazza et al. (2011) who show that the fraction of turbulent energy to thermal energy increases with decreasing time since major merger. This evolution in the thermal energy has important implications for the behavior of cluster mass proxies such as the integrated SZ flux (e.g. Nagai 2006; Shaw et al. 2008; Yang et al. 2010) or X-ray temperature (e.g. Ritchie & Thomas 2002; Rowley et al. 2004; Rasia et al. 2011) which are sensitive to the thermal energy content of the ICM, and will be explored in greater detail in future work.

It is interesting to ask at what point the large bulk velocities associated with the merger progenitors reach equilibrium with the new gravitational potential. We produce a corrected mass estimate, M_{tot} , using Equation 3 and measuring the terms due to random motions and rotation.

The lower right panel of Figure 5 shows the evolution of M_{tot} following the merger. The period up to ≈ 2 Gyr following the merger shows rapid evolution, with the mass bias ranging from a positive 20% bias to a negative 10% bias. This is driven primarily by the evolution in M_{HSE} caused by the outwardly propagating merger shock seen in Figure 1. The mean M_{tot} after 4 Gyr is essentially unbiased, with a mean of 0.3% and $\approx 8\%$ scatter at r_{500} . This indicates that the velocities at this radius have reached equilibrium with the cluster potential.

4.1. Correcting the Hydrostatic Mass Bias at $z = 0$

The dependence of M_{tot} on the time since major merger suggests a promising division between “relaxed” and “unrelaxed” clusters may be obtained by splitting a sample between objects that have and have not experienced a major merger within the past 4 Gyr. This results in a sample of 10 relaxed clusters at $z = 0$ (see Table 1).

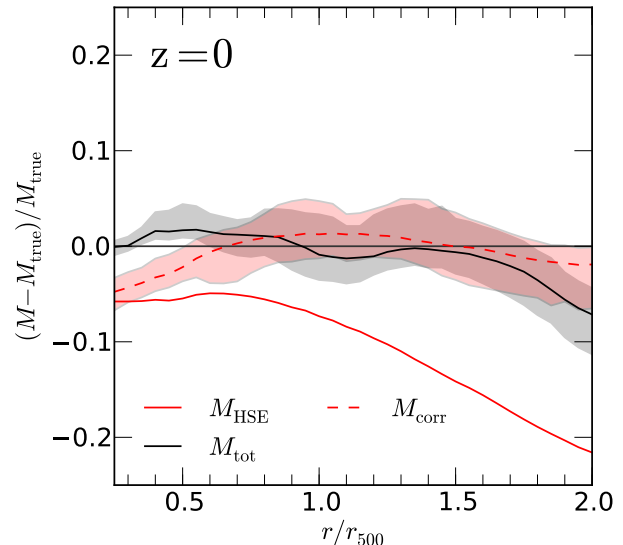


FIG. 6.— The averaged mass measurements for the relaxed subsample, split at t_{merger} of 4 Gyr at $z = 0$. We show M_{tot} (solid black) and the mass corrected using the relation from Shaw et al. (2010) fit to our subsample, M_{corr} (dashed red). See text for description of these mass calculations. M_{HSE} is shown with the solid red line for comparison.

Note that this includes all 6 clusters in Nagai et al. 07 identified as relaxed clusters based on morphological classification. Our relaxed subsample also contains an additional 4 clusters that were missed by the morphological classification scheme. This suggests that these clusters, while dynamically relaxed, appear morphologically disturbed in the X-ray images.

Figure 6 shows the average M_{HSE} (solid red line) and M_{tot} (solid black line) radial profiles for our relaxed clusters at $z = 0$. The inclusion of M_{rot} and M_{rand} in the calculation of M_{tot} removes the bias that is apparent for M_{HSE} out to $\approx 1.5r_{500}$, with a slight increase in scatter from 8% to 11% at r_{500} and 9% to 10% at r_{200} .

Since P_{rand} is not accessible observationally, we propose a model based on the average P_{rand} profile measured in our simulations. We neglect the contribution from rotation, which is $\lesssim 2\%$ of the mass correction beyond $0.7r_{500}$, and also assume velocity anisotropy, $\beta = 1 - \sigma_r^2/2\sigma_r^2$, is zero. While β is nonzero and increases radially, we find that the inclusion of β as measured from the simulations has little effect on the accuracy of our model. We parameterize the fractional contribution of the non-thermal pressure as in Shaw et al. (2010),

$$\frac{P_{\text{rand}}}{P_{\text{rand}} + P_{\text{th}}} = \alpha(r/r_{500})^n. \quad (6)$$

Using the average P_{rand} and P_{th} profiles for our relaxed sample and fitting over the radial range $0.2 \leq r/r_{500} \leq 2.0$, we obtain best fit values $\alpha = 0.14 \pm 0.09$ and $n = 1.16 \pm 0.17$. Results are mildly dependent on redshift in the redshift range $z \lesssim 0.2$ (see Shaw et al. 2010; Battaglia et al. 2011, for redshift evolution). These differ from the best fit values given in Shaw et al. (2010) of $\alpha = 0.18$ and $n = 0.8$, which were derived for the complete sample, including unrelaxed clusters. The re-

TABLE 2
MEAN BIASES IN MASS ESTIMATES AT Z=0

Mass Estimate	Sample ¹	Bias ± Scatter ²	
		r_{500}	r_{200}
M_{HSE}	Full	-0.10 ± 0.16	-0.06 ± 0.19
M_{HSE}	Relaxed	-0.07 ± 0.08	-0.14 ± 0.09
M_{tot}	Relaxed	-0.01 ± 0.11	-0.01 ± 0.10
M_{corr}	Relaxed	0.01 ± 0.09	0.00 ± 0.11

¹ Relaxed clusters are clusters that have not experienced a major merger in at least 4 Gyr.

² The error on the mean is given by the scatter divided by $\sqrt{N - 1}$, where N is a number of clusters.

sulting corrected mass profile contains only observable quantities ρ_{gas} , P_{th} , and dP_{th}/dr , and is given by

$$M_{\text{corr}} = \frac{-r^2}{G\rho_{\text{gas}}} \left(\frac{1}{1 - \alpha(r/r_{500})^n} \frac{dP_{\text{th}}}{dr} + \frac{\alpha n(r/r_{500})^{n-1}}{r_{500}(1 - \alpha(r/r_{500})^n)^2} P_{\text{th}} \right). \quad (7)$$

The dashed red line in Figure 6 shows the average M_{corr} for the sample of relaxed clusters. Using the average non-thermal pressure profile we are able to recover the true mass between $0.7-2r_{500}$. At smaller radii, $r \lesssim 0.7r_{500}$, the neglected rotational component becomes important and the mass is again underestimated. A comparison of the mean mass biases for M_{corr} and M_{HSE} at two radii are shown in Table 2. It is worth noting that the mean mass biases for both the full and relaxed subsample are in good agreement with those of Lau et al. (2009), despite differences in gas physics employed in the respective runs; i.e., non-radiative simulations in this work and the simulations including cool and star formation in Lau et al. (2009). The M_{corr} mass estimate is able to recover the true mass on average to within 1% with 10% scatter. This is a significant improvement over the mean HSE mass bias as measured for the full sample of 5–10% with 15–20% scatter.

It is important to note that this model is not applicable to unrelaxed clusters, for which the fundamental assumptions in the hydrostatic equilibrium equation do not hold. However, for the full sample, we find that the mass bias is nearly constant with very little radial dependence, which is in agreement with previous work (e.g. Battaglia et al. 2011). Applying a constant mass correction of 10% (equivalent to using our model with parameter values $\alpha = 0.1$ and $n = 0$), as has been done previously (e.g. Mantz et al. 2008), will remove the bias on average for a sample including both relaxed and unrelaxed clusters. The scatter in this correction is large, however, at 15–20%. Therefore, our correction, though only applicable to a subsample, can provide significant improvements to the cluster mass measurements when such a subsample is applicable, such as gas fraction measurements (Allen et al. 2008; LaRoque et al. 2006). We note that the correction should in principle be a function of redshift, as the contribution of non-thermal pressure grows to higher redshift when clusters are dynamically younger (e.g. Battaglia et al. 2011; Shaw et al. 2010). However, since we do not sample the full accretion histories of clusters at all redshifts, we report best fit values for our model only at $z = 0$.

5. DISCUSSION AND CONCLUSIONS

Using high-resolution adaptive mesh refinement cosmological simulations of a sample of sixteen clusters, we have performed an analysis of the effect of major mergers on the hydrostatic mass estimate. Rather than examining the properties of galaxy clusters at a single epoch, we utilize merger trees to follow the evolution of individual objects during and after mergers. We focused specifically on the characteristic features of the hydrostatic mass bias during the merger and the subsequent evolution of the random ICM motions produced.

Our principal results can be summarized as follows:

- Major mergers are the dominant sources of bulk motions providing non-thermal pressure support in the ICM and therefore bias in the hydrostatic mass estimate.
- Well after a major merger, the hydrostatic mass estimate underestimates the true mass within r_{500} by 6–10%.
- During a major merger, random kinetic motions contribute ∼30% of the total ICM pressure at r_{500} . Subsequently, the energy in these motions are converted to thermal energy over time, comprising a residual 10% contribution when the cluster is well relaxed.
- We provide a method for correcting the hydrostatic mass estimate for relaxed clusters based on the thermal pressure profile that recovers the true mass within ∼10% from $0.7-2r_{500}$.

In detail, we find the evolution of the hydrostatic mass bias can be divided into two epochs. During the merger, the infall of the smaller structure generates asymmetrical shocks that emanate from the center of the parent cluster. These shocks result in a mass bias peak that propagates outward over the course of a Gyr until it reaches the edge of the cluster.

As the clusters relax, the hydrostatic mass bias evolves more slowly, decreasing from ∼20% to 6–10% within r_{500} . Even after 8 Gyr, the mass bias in the innermost regions ($< r_{2500}$) fluctuates around 3%. The mass bias increases with increasing radius, reaching 18–20% at r_{200} , which is in agreement with previous simulations (e.g., Kay et al. 2004; Rasia et al. 2006; Nagai et al. 2007b; Lau et al. 2009) and observations (e.g., Mahdavi et al. 2008; Zhang et al. 2010).

The evolution of the hydrostatic mass bias in the second epoch, after the merger, is driven by non-thermal pressure support from bulk motions. The random kinetic energy decays after the merger, thermalizing into the surrounding ICM. Despite continued accretion, the fraction of total ICM energy in residual bulk motions falls from ∼10% immediately following the merger to ∼5% long after. Partly this reflects the inability of smoothly accreted material to excite new motions in the ICM and partly the thermalization of existing random motions. The increase in the thermal energy drives the observed decrease in the hydrostatic mass bias.

Since the bulk motions in the ICM drive the hydrostatic mass bias, we investigated methods for improving the mass estimate by accounting for the non-thermal pressure provided by random gas motions.

Within 4 Gyr of a major merger, a cluster has not yet virialized and is not in equilibrium. However, after this time, a cluster has sufficiently relaxed that with accurate treatment of the random pressure, we are able to recover the true mass. We therefore use this criteria to split our sample into “relaxed” and “unrelaxed” by dividing into clusters that have and have not experienced a major merger in the last 4 Gyr.

We provide a method for correcting the hydrostatic mass estimate for relaxed clusters by harnessing the similarity in the evolution of the non-thermal pressure profiles. This method combines the true thermal pressure profile for each cluster individually with the average non-thermal pressure profile of the relaxed sample. At $z = 0$, our model recovers the true mass to within $\sim 10\%$ in the radial range $0.7\text{--}2 r_{500}$.

There are a few issues to bear in mind when interpreting our results. First, our simulations neglect radiative cooling, energy feedback from stars and active galactic nuclei, and additional sources of non-thermal pressure such as cosmic-rays and magnetic field. While these effects are critical for cluster cores, their effects on cluster outskirts remain uncertain and must be explored in the future studies. Uncertainty in our results may also arise from the lack of viscosity and our treatment of the ICM as a single fluid, neglecting various effects important for plasmas. Finally, our measurements use full three dimen-

sional information from the simulations averaged using spherical symmetry and therefore do not account for projection effects. We exclude gas contained within subhalos of mass greater than $10^{12} h^{-1} M_\odot$, which will differ somewhat from observationally identified peaks in emission. These differences may account for our somewhat smaller mass biases than those measured from mock X-ray analyses (e.g. Nagai et al. 2007b; Rasia et al. 2004). However, despite these caveats, we are confident that it is possible to gain better control on the bias in the hydrostatic mass estimate of clusters by taking into account its dependence on dynamical state. In the future work, we will explore possible morphological classification schemes for defining these subsamples based on observational data.

We thank Erwin Lau and Andrey Kravtsov for useful discussions. We also acknowledge the anonymous referee for valuable feedback on the manuscript. This work was supported in part by NSF grant AST-1009811, by NASA ATP grant NNX11AE07G, and by the facilities and staff of the Yale University Faculty of Arts and Sciences High Performance Computing Center. D.H.R. acknowledges the support of NSF grant OCI-0904484. The simulations used in this study were performed on the BulldogM cluster at the Yale University Faculty of Arts and Sciences High Performance Computing Center.

REFERENCES

- Allen, S. W., Rapetti, D. A., Schmidt, R. W., Ebeling, H., Morris, R. G., & Fabian, A. C. 2008, Monthly Notices of the Royal Astronomical Society, 383, 879
 Battaglia, N., Bond, J. R., Pfrommer, C., & Sievers, J. L. 2011, arXiv, astro-ph.CO
 Binney, J., & Tremaine, S. 2008, Galactic Dynamics: Second Edition, by James Binney and Scott Tremaine. ISBN 978-0-691-13026-2 (HB). Published by Princeton University Press, Princeton, NJ USA, 2008., -1
 Gottlöber, S., Klypin, A., & Kravtsov, A. V. 2001, ApJ, 546, 223
 Iapichino, L., & Niemeyer, J. C. 2008, Monthly Notices of the Royal Astronomical Society, 388, 1089
 Jeltema, T. E., Hallman, E. J., Burns, J. O., & Motl, P. M. 2008, arXiv, 681, 167
 Kaiser, N. 1986, MNRAS, 222, 323
 Kay, S. T., Thomas, P. A., Jenkins, A., & Pearce, F. R. 2004, MNRAS, 355, 1091
 Klypin, A., Gottlöber, S., Kravtsov, A. V., & Khokhlov, A. M. 1999, ApJ, 516, 530
 Klypin, A., Kravtsov, A. V., Bullock, J. S., & Primack, J. R. 2001, ApJ, 554, 903
 Kravtsov, A. V. 1999, PhD thesis, NEW MEXICO STATE UNIVERSITY
 Kravtsov, A. V., Berlind, A. A., Wechsler, R. H., Klypin, A. A., Gottlöber, S., Allgood, B., & Primack, J. R. 2004, ApJ, 609, 35
 Kravtsov, A. V., Klypin, A., & Hoffman, Y. 2002, ApJ, 571, 563
 LaRoque, S. J., Bonamente, M., Carlstrom, J. E., Joy, M. K., Nagai, D., Reese, E. D., & Dawson, K. S. 2006, ApJ, 652, 917
 Lau, E. T., Kravtsov, A. V., & Nagai, D. 2009, ApJ, 705, 1129
 Mahdavi, A., Hoekstra, H., Babul, A., & Henry, J. P. 2008, Monthly Notices of the Royal Astronomical Society, 384, 1567
 Mantz, A., Allen, S. W., Ebeling, H., & Rapetti, D. 2008, Monthly Notices of the Royal Astronomical Society, 387, 1179
 Mantz, A., Allen, S. W., Rapetti, D., & Ebeling, H. 2010, Monthly Notices of the Royal Astronomical Society, 406, no Meneghetti, M., Rasia, E., Merten, J., Bellagamba, F., Ettori, S., Mazzotta, P., Dolag, K., & Marri, S. 2010, A&A, 514, 93
 Nagai, D. 2006, ApJ, 650, 538
 Nagai, D., Kravtsov, A. V., & Vikhlinin, A. 2007a, ApJ, 668, 1
 Nagai, D., Vikhlinin, A., & Kravtsov, A. V. 2007b, ApJ, 655, 98
 Piffaretti, R., & Valdarnini, R. 2008, A&A, 491, 71
 Poole, G. B., Fardal, M. A., Babul, A., McCarthy, I. G., Quinn, T., & Wadsley, J. 2006, MNRAS, 373, 881
 Puchwein, E., & Bartelmann, M. 2007, A&A, 474, 745
 Rasia, E., Mazzotta, P., Evrard, A., Markevitch, M., Dolag, K., & Meneghetti, M. 2011, ApJ, 729, 45
 Rasia, E., Tormen, G., & Moscardini, L. 2004, MNRAS, 351, 237
 Rasia, E., et al. 2006, MNRAS, 369, 2013
 —. 2012, eprint arXiv:1201.1569
 Ricker, P. M., & Sarazin, C. L. 2001, ApJ, 561, 621
 Ritchie, B. W., & Thomas, P. A. 2002, Monthly Notices of the Royal Astronomical Society, 329, 675
 Rowley, D. R., Thomas, P. A., & Kay, S. T. 2004, Monthly Notices of the Royal Astronomical Society, 352, 508
 Rozo, E., et al. 2009, ApJ, 708, 645
 Rudd, D. H., Zentner, A. R., & Kravtsov, A. V. 2008, ApJ, 672, 19
 Sehgal, N., Bode, P., Das, S., Hernández-Monteagudo, C., Huffenberger, K., Lin, Y.-T., Ostriker, J. P., & Trac, H. 2010, ApJ, 709, 920
 Shaw, L. D., Holder, G. P., & Bode, P. 2008, ApJ, 686, 206
 Shaw, L. D., Nagai, D., Bhattacharya, S., & Lau, E. T. 2010, arXiv, astro-ph.CO
 Vanderlinde, K., et al. 2010, ApJ, 722, 1180
 Vazza, F., Brunetti, G., Heller, C., Brunino, R., & Brüggen, M. 2011, A&A, 529, A17
 Vikhlinin, A., et al. 2009, ApJS, 692, 1033
 Yang, H.-Y. K., Bhattacharya, S., & Ricker, P. M. 2010, ArXiv e-prints
 Zhang, Y.-Y., et al. 2010, ApJ, 711, 1033